



# CURVE SQUEAL OF TRAIN WHEELS, PART 1: MATHEMATICAL MODEL FOR ITS GENERATION

MARIA A. HECKL AND I. D. ABRAHAM<sup>†</sup>

*Department of Mathematics, Keele University, Keele, Staffordshire ST5 5BG, England*

*(Received 25 August 1998, and in final form 5 August 1999)*

A mathematical model is presented for the squeal noise generated by trains when traversing tight curves. Curve squeal is presumed to arise from lateral crabbing of the wheels across the rail head. This induces a lateral friction force acting at the contact of each wheel with the rail. An individual wheel then performs out-of-plane oscillations which are radiated and heard as squeal. This phenomenon is modelled by considering a flat round disc, with several out-of-plane modes, excited at one point along the edge by a dry-friction force (typically a stick/slip force) which is dependent on the disc velocity. An iteration scheme is developed which gives the time history of the disc velocity. The iteration is straightforward and only requires the impulse response (or the Green's function) of the disc and the functional dependence between friction force and disc velocity (friction characteristic). The numerical simulations produce time histories that show transient phenomena, such as exponential amplitude growth and the onset of limit cycles. The way these phenomena are influenced by some parameters, in particular the modal loss factors of the disc and its crabbing speed, will be examined. Practical methods to reduce or eliminate curve squeal will be discussed.

© 2000 Academic Press

## 1. INTRODUCTION

When a train goes round a tight curve, it often emits an intense high-pitched squeal, a familiar, but very unpleasant, noise. This noise is the sound radiated from individual wheels that are excited by the dry friction forces that are associated with a sliding of the wheels against the rail.

It is generally accepted that “wheel crabbing” (a term coined by Rudd [1]) is responsible for the generation of curve squeal. Wheel crabbing occurs when a truck with two (or more) rigid parallel axles negotiates a curve. Its wheels cannot align themselves tangentially to the rail; instead, the wheels on the front axle tend to run out of the curve, and those on the trailing axle tend to run into the curve (see Figure 1). The speed of an individual wheel has two components: the rolling speed

<sup>†</sup>Present address: Department of Mathematics, University of Manchester, Oxford Road, Manchester M13 9PL, England.

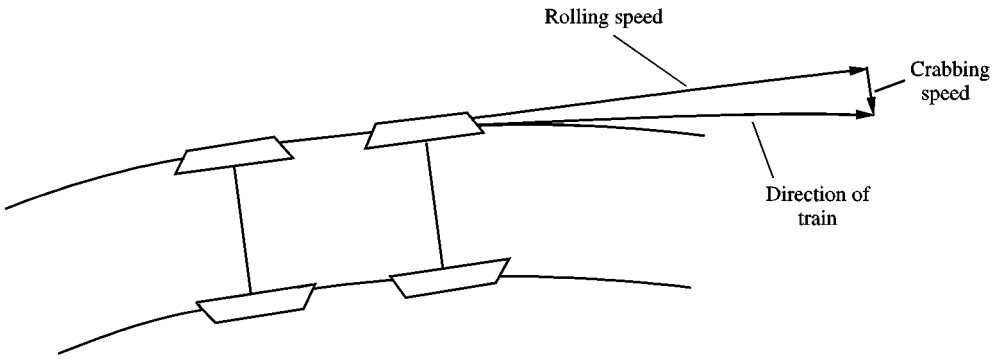


Figure 1. Crabbing of a truck in a curve.

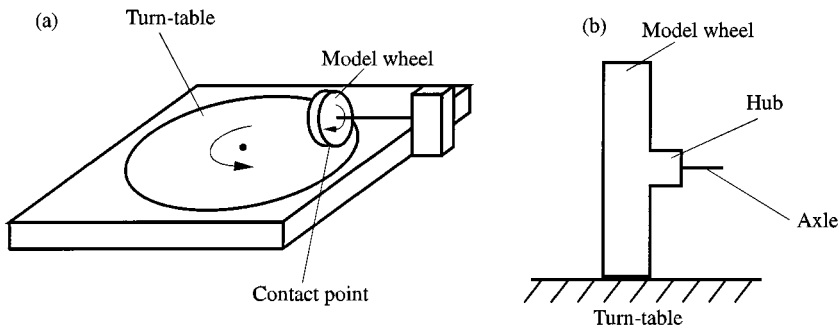


Figure 2. Model rig to simulate wheel crabbing: (a) perspective view; (b) side-view.

which is tangential to the wheel, and the crabbing speed which is perpendicular to the wheel and depends on the angle between the wheel and rail. This crabbing motion induces a friction force which is normal to the plane of the wheel. This normal force excites out-of-plane or bending oscillations of the wheel. A wheel performing bending oscillations is a very efficient radiator of sound, and this is one reason for the high intensity of curve squeal. An alternative to the term “wheel crabbing” is used in the railway engineering community and contact mechanics fraternity; there the expression “wheels with high angles of attack” is commonly used.

The model rig shown schematically in Figure 2 simulates curve squeal due to wheel crabbing. The model wheel is a flat circular disc with a straight edge perpendicular to the plane of the disc. It is held at the centre, but allowed to rotate, and rolls on a turn-table which represents the rail. If the wheel is tangential to its circular path on the turn-table, no crabbing takes place. If, however, the wheel has a non-tangential alignment, crabbing with a constant lateral speed occurs. The friction force generated in this way is normal to the plane of the model wheel and excites bending oscillations that are radiated from the wheel into the surrounding air.

The frequency spectrum of curve squeal typically has between one and four sharp peaks that correspond to certain bending resonances of the wheel. These

resonances are “self-excited”, i.e., the friction force which drives the wheel motion is itself dependent on the wheel motion. The functional dependence between friction force and wheel velocity is called the “friction characteristic”, and it is an essential feature for the generation of squeal noise. For example, a linear friction characteristic, where the friction force rises with the wheel velocity, represents a force with negative damping, and it is intuitively obvious, that this would lead to an unstable self-excited oscillation. A more realistic friction characteristic is one that describes stick/slip, as it is generally accepted that squeal is associated with a stick/slip mechanism where the friction force oscillates in rapid succession between sliding friction and rolling friction.

The generation mechanism of curve squeal is analogous to that of the bowed string. A bow is drawn perpendicularly and with constant speed (equivalent to the crabbing speed) across the string, and the friction force generated in this way drives oscillations of the string. This system has been studied in detail by McIntyre and Woodhouse [2]. Our approach is close to theirs in two ways. We calculate time histories for the wheel motion from an iteration procedure in the time domain, and we presume that the friction force is described by a friction characteristic that is a piecewise linear version of the one they use.

Curve squeal has been much investigated theoretically and experimentally. Von Stappenbeck [3] was the first to propose wheel crabbing as the mechanism relevant for the generation of curve squeal. Important contributions were made by Rudd [1] who recognized that the friction acts like a force with negative damping and thus drives unstable wheel oscillations. He developed a theoretical model for a single-mode wheel and also considered non-linear effects in the friction force to estimate the stable wheel vibration amplitude. In a comprehensive review article, Remington [4] described the state of knowledge up to 1985.

Since then, a number of increasingly sophisticated models for wheel/rail squeal, consisting of various submodels, have been published. For example, Schneider *et al.* [5] examined the generation of squeal, developing submodels for the wheel (modal model), friction force (featuring negative damping and non-linearity) and sound power radiation (based on the Rayleigh integral for a baffled radiator). The wheel is described by modal co-ordinates, which are calculated from non-linear differential equations in time. Fingberg’s model [6] is more advanced and consists of submodels for the wheel set (finite element model), friction force (from detailed contact-mechanical considerations), rail model (modal model) and sound power radiation (boundary element method). Fingberg’s work has been extended further by Périard [7], who included a submodel for the train body and considered more complicated wheel designs. Périard treated curve squeal as a transient phenomenon with irregular motion as the train enters or leaves the curve.

Within the applied mathematics community, friction-driven systems have served as case studies for the application of dynamical systems analysis. There is a substantial number of publications, typically studying systems with one or two degrees of freedom (d.o.f.s). For example, Popp and Stelter [8] report theoretical studies of one- and two-d.o.f. mass/spring oscillators which are excited by different types of friction characteristic. Their simulations focus on the transitions from regular to chaotic motion. McMillan [9] has performed simulations on a mass/

spring oscillator driven by hysteretical friction forces and examined the influence of initial conditions.

This paper is directed at the acoustic engineering as well as the applied mathematics community. Our aim is to model the test rig shown in Figure 2 with a combined analytical/numerical approach. We take into account several wheel modes, rather than just one or two d.o.f.s. However, we do not aim to simulate precisely the geometrical details of a real train wheel or to improve the accuracy of existing comprehensive numerical models. Our mathematical treatment involves the Green's function (or impulse response) of the free wheel and the friction characteristic. We thus look at wheel/rail squeal from a new and different perspective to give new insight and to complement the more engineering-oriented numerical models.

The mathematical model will be formulated in Section 2 in terms of an integral equation. The theoretical calculation of the Green's function of our model wheel will be shown in Section 3. An iteration scheme to solve the integral equation is derived in Section 4. The time histories resulting from this iteration are shown and discussed in Section 5. Section 6 focuses on methods to control squeal; various practices in the railway industry are discussed in the light of our simulations.

## 2. GENERAL FORMULATION OF THE MATHEMATICAL MODEL

We consider the set-up shown in Figure 2. The wheel is represented by a circular plate or disc. The contact patch is assumed to be just a single point  $(r', \varphi')$  along the circumference of the disc. At this point, the friction force acts. The crabbing of the disc takes place with a constant speed  $V$ . In addition to the crabbing, the disc performs bending oscillations with a velocity  $v$  that depends on the position  $(r, \varphi)$  on the disc. The rotation of the wheel is neglected.

### 2.1. THE FRICTION CHARACTERISTIC

The friction characteristic is the functional dependence between the friction force and the relative motion between the two bodies in contact. It depends on various parameters, such as material and surface properties, normal load, relative velocity, and we denote the friction characteristic by  $F(v)$ . We confine ourselves to working with assumed friction characteristics, without getting into the mechanics of the contact patch or the physics of dry-friction forces. Two different friction characteristics, depicted in Figure 3(a) and (b), will be used; they are idealizations of measured friction characteristics and it will turn out that they have features that are important for the generation and the intensity of squeal noise.

Figure 3(a) shows a linear friction characteristic,  $F(v) = F_0 + \gamma v$ .  $F_0$  is a constant component, and  $\gamma v$  is a component which oscillates due to the time dependence of  $v$ , the disc velocity at the contact point. The positive slope  $\gamma$  in the friction characteristic represents a negative damping coefficient.

The friction characteristics in Figure 3(b) are marked by a strong non-linearity and represent stick/slip. The very steep section located around the crabbing speed

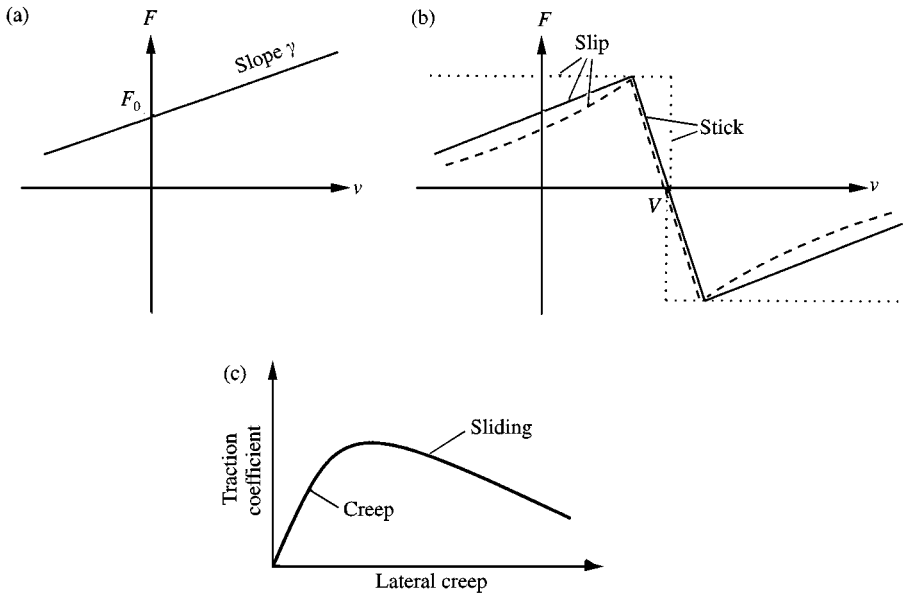


Figure 3. Friction characteristics ( $F$ : friction force,  $v$ : disc velocity at the contact point,  $V$ : crabbing speed); (a) linear friction characteristic,  $F(v) = F_0 + \gamma v$ ; (b) friction characteristic of a bowed string (dashed line), piecewise linear approximation (solid line) and Coulomb friction (dotted line); (c) creep curve.

$V$  represents sticking. This is a state where the roughness peaks of the contacting bodies form temporary bonds and the friction force is due to elastic forces exerted by the distorted roughness peaks. On either side of  $V$  is a slip section, which is marked by a rather gentler slope. This is a state where the bonds between the roughness peaks have been disrupted and a sliding motion over a distance much larger than the width of the roughness peaks takes place.

The Coulomb friction law is shown by the dotted line in Figure 3(b). The dashed line in Figure 3(b) is the friction characteristic used by McIntyre and Woodhouse [2]. The solid, piecewise linear, curve in Figure 3(b) is of interest in two ways: it is an approximation of the bowed-string force, and it is a generalization of the linear curve in Figure 3(a) which is only valid for cases where the wheel velocity  $v$  never reaches the crabbing speed  $V$ , i.e., where sticking never takes place.

In the contact mechanics community, the friction characteristic is more commonly given in terms of a creep curve, where the traction coefficient (ratio between the magnitudes of friction force and normal load) is given as a function of lateral creep (ratio between sliding velocity across the rail and rolling velocity). A typical creep curve, which corresponds to our stick/slip friction characteristic is shown in Figure 3(c). The following steps would convert qualitatively from our friction characteristic (solid line in Figure 3(b)) to that shown in Figure 3(c).

- Shift the curve to the left so that the zero of  $F$  lies at the origin (equivalent to plotting  $F$  against the relative velocity  $v - V$ , instead of the wheel velocity  $v$ ).
- Consider only the left-hand part of the curve, where the relative velocity is negative, and reflect it about the force axis (equivalent to ignoring the sign

difference between friction force and relative velocity and plotting only their magnitudes).

- Scale the velocity axis with the rolling velocity (equivalent to converting from relative velocity to creep).
- Scale the force axis with the normal load (equivalent to converting from friction force to traction coefficient).

The instability-inducing feature in the creep curve is the negative gradient for creepages beyond the point of saturated creep.

## 2.2. THE GREEN'S FUNCTION OF THE FREE DISC

We consider a free disc which has no contact that might induce friction. If this disc is hit at time  $t'$  by a point force at point  $(r', \varphi')$ , then the displacement at some later time  $t$  and at any observer point  $(r, \varphi)$  is given by the Green's function or impulse response

$$G(r, \varphi; r', \varphi'; t - t') = \begin{cases} \text{real} \sum_{m=0}^{\infty} \sum_{n=1}^{\infty} g_{mn}(r, \varphi; r', \varphi') e^{-i(\omega_{mn} + i\delta_{mn})(t - t')} & \text{for } t \geq t', \\ 0 & \text{for } t < t'. \end{cases} \quad (2.1a, b)$$

Equation (2.1a) represents a superposition of bending modes with mode numbers  $(m, n)$ .  $m$  determines the number of nodal lines and  $n$  the number of nodal circles (or points);  $\omega_{mn}$ ,  $\delta_{mn}$  and  $g_{mn}$  are respectively the allowed frequency, growth rate and amplitude corresponding to mode  $(m, n)$ . Before the impulse strikes, the disc is in a state of rest with zero displacement; this is described by equation (2.1b).

The Green's function can be determined theoretically (see Section 3) or experimentally by measuring the disc response to an impulse point force.

## 2.3. THE SUPERPOSITION PRINCIPLE

The free disc is treated here as a linear system. Its response to a single impulse force is known; it is given by the Green's function. Then the response of a series of impulse forces (simulating the time history  $F(t')$  of a continuous force) is given by a linear superposition of the responses to the individual impulses. This can be expressed by the following integral:

$$w(r, \varphi, t) = \int_{t'=0}^t F(t') G(r, \varphi; r', \varphi'; t - t') dt', \quad (2.2)$$

where  $w$  is the disc displacement that results from a force  $F$  that starts acting at time  $t' = 0$ . The force relevant here is the friction force, and is related to the disc velocity

$v$  by a friction characteristic  $F(v)$ . Then equation (2.2) becomes (after differentiation with respect to time  $t$ , using  $v = \dot{w}$  and  $G(r, \varphi; r', \varphi'; 0) = 0$ )

$$v(r, \varphi, t) = \int_{t'=0}^t F(v(r', \varphi', t')) \frac{\partial G(r, \varphi; r', \varphi'; t - t')}{\partial t} dt'. \tag{2.3}$$

This represents an integral equation (of the Volterra type) for the disc velocity  $v$ . In Section 4, the time history of  $v$  will be calculated by an iteration stepping forward in time.

### 3. THEORETICAL CALCULATION OF THE GREEN'S FUNCTION OF A FREE-EDGED DISC CLAMPED AT THE CENTRE

We consider an annular disc (see Figure 4) with uniform thickness; the outer edge of the disc is free, the inner edge clamped. The Green's function of the disc is the time history of the disc displacement that results from an impulse point force. Its governing equation is

$$B\nabla^4 G + M \frac{\partial^2 G}{\partial t^2} = \delta(t - t')\delta(r - r')\delta(\varphi - \varphi'). \tag{3.1}$$

The position and time of the force are denoted by primes ( $r', \varphi'$ ) and  $t'$ , while the time and position of the observer, ( $r, \varphi$ ) and  $t$ , have no primes.  $B$  is the bending

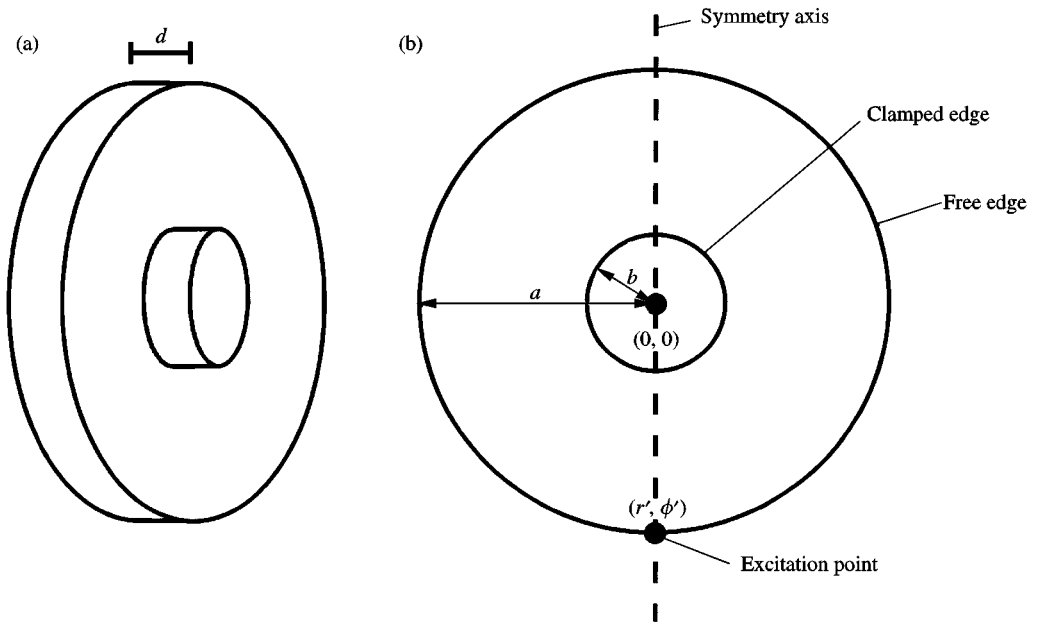


Figure 4. Annular disc with a free outer edge and clamped inner edge, excited by a point force.

stiffness per unit area of the disc; for a disc with Young's modulus  $E$ , thickness  $d$  and the Poisson ratio  $\nu$ ,  $B$  is given by  $B = Ed^3/12(1 - \nu^2)$ .  $M$  is the mass per unit area of the disc.

The boundary conditions for a circular plate with a clamped inner edge of radius  $b$  and a free outer edge of radius  $a$  (see Figure 4) in polar co-ordinates are

$$G = 0 \quad \text{at} \quad r = b, \quad (3.2a)$$

$$\frac{\partial G}{\partial r} = 0 \quad \text{at} \quad r = b, \quad (3.2b)$$

$$\frac{\partial^2 G}{\partial r^2} + \frac{\nu}{a} \left( \frac{\partial G}{\partial r} + \frac{1}{a} \frac{\partial^2 G}{\partial \varphi^2} \right) = 0 \quad \text{at} \quad r = a, \quad (3.2c)$$

$$\frac{\partial^3 G}{\partial r^3} + \frac{1}{a} \frac{\partial^2 G}{\partial r^2} - \frac{1}{a^2} \frac{\partial G}{\partial r} + \frac{2 - \nu}{a^2} \frac{\partial^3 G}{\partial r \partial \varphi^2} - \frac{3 - \nu}{a^3} \frac{\partial^2 G}{\partial \varphi^2} = 0 \quad \text{at} \quad r = a. \quad (3.2d)$$

Equations (3.2a) and (3.2b) represent the clamping at the inner edge where the lateral displacement and its slope in the radial direction have to be zero. The other two equations (from reference [10, p. 359]) represent the boundary conditions at the free outer edge, where the bending moment (equation (3.2c)) and the shearing force (equation (3.2d)) have to be zero.

The approach to solve the non-homogeneous boundary value problem made up by equations (3.1) and (3.2a)–(3.2d) for the Green's function is shown in Appendix A. The solution is of the form

$$G(r, \varphi; r', \varphi'; t - t') = \begin{cases} \text{real} \sum_{m=0}^{\infty} \sum_{n=1}^{\infty} R_{mn}(r) A_{mn}(r') \cos m(\varphi - \varphi') e^{-i\omega_{mn}(t-t')} & \text{for } t \geq t', \\ 0 & \text{for } t < t'. \end{cases} \quad (3.3)$$

The  $r$ -dependent part  $R_{mn}(r)$  is

$$R_{mn}(r) = J_m(k_{mn}r) + B_{mn} I_m(k_{mn}r) + C_{mn} Y_m(k_{mn}r) + D_{mn} K_m(k_{mn}r). \quad (3.4)$$

$J_m$  and  $Y_m$  are the Bessel and Neumann functions respectively of order  $m$ ; their behaviour is roughly sinusoidal.  $I_m$  and  $K_m$  are the hyperbolic (or modified) Bessel functions of order  $m$ ; their behaviour is roughly exponential. The functions  $Y_m$  and  $K_m$  have a singularity at  $r = 0$  (see reference [11, Chapter 9]), but they are included because the centre  $r = 0$  is not a part of the vibrating surface.  $B_{mn}$ ,  $C_{mn}$  and  $D_{mn}$  are relative amplitudes; they are given by lengthy expressions in terms of the Bessel

functions, Neumann functions, hyperbolic Bessel functions and the derivatives of them all (see Appendix A).

$k_{mn}$  are the allowed wave numbers; they are the solutions of a lengthy non-linear algebraic equation (see Appendix A).  $\omega_{mn}$  are the allowed frequencies,

$$\omega_{mn} = k_{mn}^2 \sqrt{\frac{B}{M}}. \tag{3.5}$$

The  $r'$ -dependent part of equation (3.3),  $A_{mn}(r')$ , is given by

$$A_{mn}(r') = -\frac{r' R_{mn}(r')}{M i \omega_{mn} \varepsilon_m \pi \int_{r=b}^a R_{mn}^2(r) r dr}, \tag{3.6a}$$

with

$$\varepsilon_m = \begin{cases} 2 & \text{for } m = 0, \\ 1 & \text{for } m \neq 0. \end{cases} \tag{3.6b}$$

Thus, the Green's function amplitudes in (2.1a) are

$$g_{mn}(r, \varphi; r', \varphi') = R_{mn}(r) A_{mn}(r') \cos m(\varphi - \varphi'), \tag{3.7}$$

and the corresponding allowed frequencies  $\omega_{mn}$  are specified in equation (3.5). The damping  $\delta_{mn}$  of individual modes cannot be calculated by this approach; it would require a more sophisticated model, taking internal and radiation damping of the disc into account.

#### 4. SOLUTION OF THE INTEGRAL EQUATION BY ITERATION

This section develops a method to calculate the time history of the disc motion, in particular that of the velocity at the force point  $(r', \varphi')$ . We start with the integral equation (2.3) and insert the time derivative of the Green's function, using equation (2.1a). The resulting equation is evaluated at the force point  $(r', \varphi')$  to give the velocity at that point,

$$v(t) = \text{real} \left( \sum_{m=0}^{\infty} \sum_{n=1}^{\infty} -i \psi_{mn} g_{mn} e^{-i\psi_{mn}t} \int_{t'=0}^t F(v(t')) e^{i\psi_{mn}t'} dt' \right). \tag{4.1}$$

The complex frequency  $\psi_{mn}$  has been introduced to denote

$$\psi_{mn} = \omega_{mn} + i\delta_{mn}. \tag{4.2}$$

The integral in equation (4.1),

$$I_{mn}(t) = \int_{t'=0}^t F(v(t')) e^{i\psi_{mn}t'} dt', \tag{4.3}$$

can be split into two parts, one over the interval  $(0, t - \Delta t)$ , and the other over an interval of width  $\Delta t$ , where  $\Delta t$  is a small time step,

$$I_{mn}(t) = \int_{t'=0}^{t-\Delta t} F(v(t')) e^{i\psi_{mn}t'} dt' + \int_{t'=t-\Delta t}^t F(v(t')) e^{i\psi_{mn}t'} dt'. \quad (4.4)$$

The first integral represents  $I_{mn}(t - \Delta t)$ . The second integral can be approximated: the time interval  $\Delta t$  is assumed to be very small, and therefore the force in this interval is nearly constant and equal to  $F(v(t - \Delta t))$ ; the integral can then be calculated analytically as  $F(v(t - \Delta t)) (e^{i\psi_{mn}t} / i\psi_{mn}) (1 - e^{-i\psi_{mn}\Delta t})$ . With these results, equation (4.4) can be written as

$$I_{mn}(t) = I_{mn}(t - \Delta t) + F(v(t - \Delta t)) \frac{e^{i\psi_{mn}t}}{i\psi_{mn}} (1 - e^{-i\psi_{mn}\Delta t}), \quad (4.5)$$

and this leads with equation (4.1) to

$$v(t) = \text{real} \sum_{m=0}^{\infty} \sum_{n=1}^{\infty} -i\psi_{mn} g_{mn} e^{-i\psi_{mn}t} I_{mn}(t). \quad (4.6)$$

Equations (4.5) and (4.6) comprise an iteration procedure for the time history of the velocity  $v(t)$ , stepping forward in time with steps  $\Delta t$ . It starts at time  $t = 0$ , where the initial condition  $I_{mn}(0) = 0$  (equivalent to  $v(0) = 0$ ) provides the starting point for the iteration.

The iteration succeeds not just for linear friction characteristics, but for any friction characteristic  $F(v)$ .

In the numerical implementation of this iteration procedure only a finite number of modes can be considered. The mode with the largest frequency imposes an upper limit on the time step:  $\Delta t$  has to be smaller than the period of that mode.

## 5. NUMERICAL RESULTS

### 5.1. PROPERTIES OF THE FREE DISC

In our numerical simulations we considered a steel disc with the following material properties:  $\rho = 8000 \text{ kg/m}^3$  (mass density),  $E = 2 \times 10^{11} \text{ N/m}^2$  (Young's modulus),  $\nu = 0.3$  (Poisson ratio), and the following geometry:  $d = 0.003 \text{ m}$  (disc thickness),  $a = 0.038 \text{ m}$  (disc radius),  $b = 0.01 \text{ m}$  (radius of inner ring where the disc is clamped).

Table 1 shows the eigenfrequencies  $f_{mn}$  and the Green's function amplitudes  $g_{mn}$  for the disc. These values were calculated using the method described in Section 3 and in Appendix A.

Only the first five modes ( $m = 0, \dots, 4, n = 1$ ) have eigenfrequencies within the range of audible frequencies, and only those modes were included in the numerical

TABLE 1

*Eigenfrequencies and the Green's function amplitudes for some low modes of the considered disc*

$m$	$n$	$f_{mn}$ (Hz)	real ( $g_{mn}$ )	imag ( $g_{mn}$ ) ( $10^{-9}$ m/N s)
0	1	3020	0	1969
1	1	2922	0	4124
2	1	3655	0	3472
3	1	6482	0	2141
4	1	10980	0	1409
5	1	16770	0	1020
0	2	19170	0	307
1	2	20220	0	580
2	2	23560	0	490
3	2	29500	0	379
4	2	38050	0	287
5	2	48860	0	224

simulations of the friction-driven disc. The vibration patterns of these modes are shown in Figure 5.

Preliminary experiments have been performed on the rig shown in Figure 2. The rig has a steel model wheel like the one studied here: it is a flat disc with a hub at the centre and has the above values for the geometry parameters  $d$ ,  $a$  and  $b$  (hub radius). The Green's function of the model wheel has been measured and is shown in Figure 6. The wheel squeals at a frequency of about 6800 Hz. Experiments, where the wheel was excited at various frequencies and sprinkled with sugar to visualize the vibration pattern, revealed that this is the eigenfrequency of mode (3, 1).

## 5.2. MOTION OF THE FRICTION-DRIVEN DISC

The time histories of the disc velocity (at the contact point) and of the friction force were calculated with the iteration scheme of equations (4.5) and (4.6). The iteration requires the complex eigenfrequencies  $\psi_{mn}$  and the Green's function amplitudes  $g_{mn}$ . The complex eigenfrequencies were taken to be  $\psi_{mn} = 2\pi f_{mn}(1 - i\eta_{mn})$ , where  $f_{mn}$  are the real eigenfrequencies, listed in Table 1, and  $\eta_{mn}$  are modal loss factors. In the numerical simulations, the modal loss factors were varied to find out their influence on the disc motion. The Green's function amplitudes  $g_{mn}$  were also taken from Table 1.

The iteration was started with zero velocity as the initial condition, progressing with time steps  $\Delta t = 6 \times 10^{-6}$  s. This time step is considerably smaller (by a factor of 1/15) than the period of mode (4,1) which has the highest frequency.

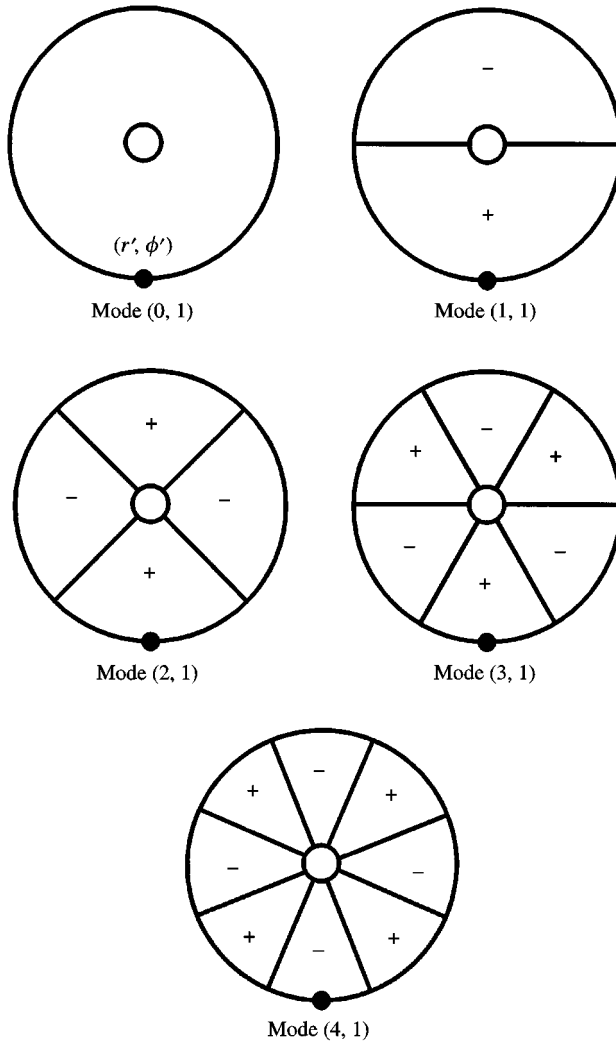


Figure 5. Vibration patterns of the first five modes.

Two friction characteristics were considered: the linear friction characteristic (see Figure 3(a)), given by

$$F(v) = F_0 + \gamma v, \tag{5.1}$$

and the non-linear friction characteristic (see Figure 3(b), solid line), given by

$$F(v) = \begin{cases} F_0 + \gamma v & \text{for } v < V - \Delta V \text{ and } v > V + \Delta V \text{ (slip),} \\ \Gamma(v - V) & \text{for } v \in (V - \Delta V, V + \Delta V) \text{ (stick).} \end{cases} \tag{5.2}$$

The following numerical values were used for the parameters in equation (5.1) and (5.2):  $\gamma = 15\,000 \text{ N s/m}$  (slope of the slip section),  $\Gamma = -100\,000 \text{ N s/m}$  (slope of the

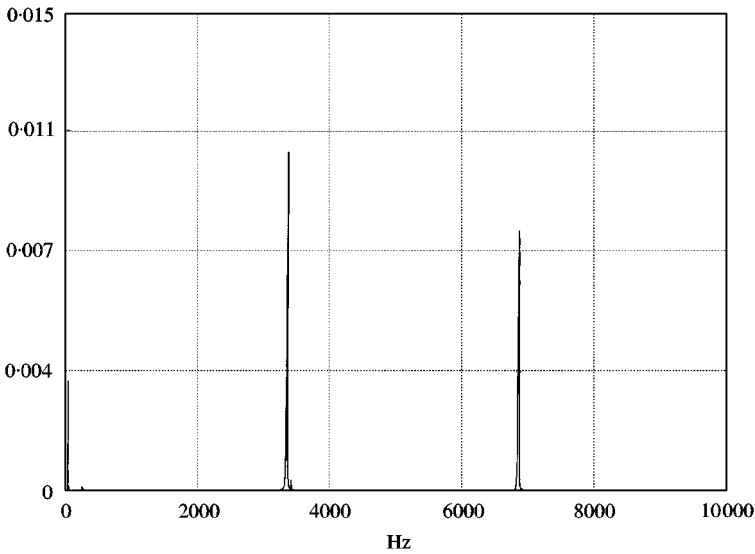


Figure 6. Spectrum of the measured the Green's function of the model wheel.

stick section),  $V = 50 \times 10^{-6}$  m/s (crabbing speed).  $\Delta V$  is the narrow velocity interval which encloses the stick section of the friction characteristic.  $F_0$  is assumed to be equal to the vertical force exerted at the contact point by the weight of the disc,

$$F_0 = M_d g \quad \text{with} \quad M_d = 0.109 \text{ kg and } g = 9.81 \text{ m/s}^2.$$

This gravitational force on the model wheel is the minimum for  $F_0$ . In most situations, it needs to be supplemented, e.g., by the gravitational force acting on train components other than the wheel.

Figures 7(a)–(d) (linear friction characteristic) and 8(a)–(d) (non-linear friction characteristic) show the time histories for the different sets of modal loss factors listed in Table 2. The solid curves give the time history of the velocity and the dashed curves that of the friction force. The co-ordinate labels along the vertical axis of these figures are for the velocity (in  $10^{-6}$  m/s).

### 5.3. DISCUSSION OF THE NUMERICAL RESULTS

Simulations using the linear friction characteristic (5.1) lead to unstable oscillations with indefinitely growing amplitudes (see Figure 7(a)–(d)). Mode (2, 1) is unstable in Figure 7(a); mode (3, 1) is unstable in Figure 7(b); modes (2, 1) and (3, 1) are unstable, with mode (3, 1) dominating, in Figure 7(c); modes (2, 1) and (3, 1) are about equally unstable in Figure 7(d).

The two most crucial parameters for the stability behaviour are the modal loss factors  $\eta_{mn}$  and the slope  $\gamma$  of the linear friction characteristic. The figures indicate clearly that a decrease of  $\eta_{mn}$  of any one mode has a destabilizing effect on this mode. The slope  $\gamma$  has been kept constant in the figures shown here. Simulations

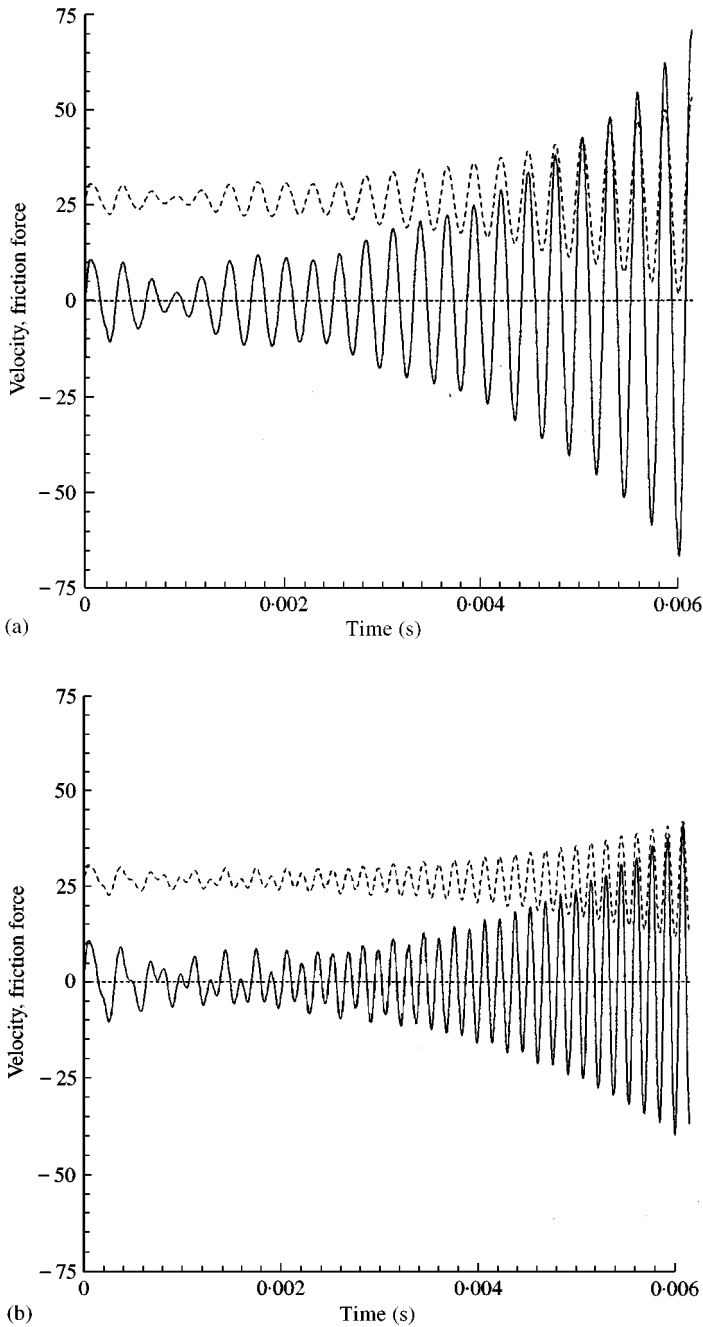


Figure 7. Time histories of the disc velocity (solid curve) and friction force (dashed curve); linear friction characteristic.

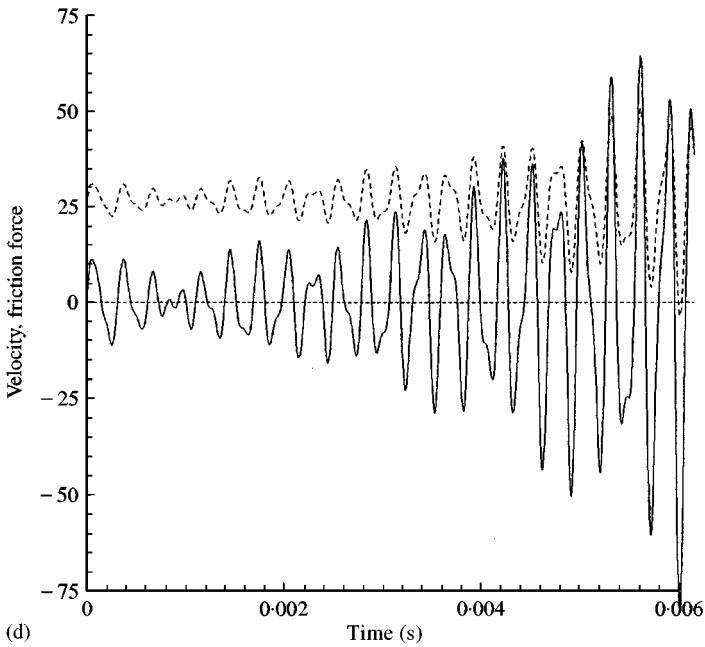
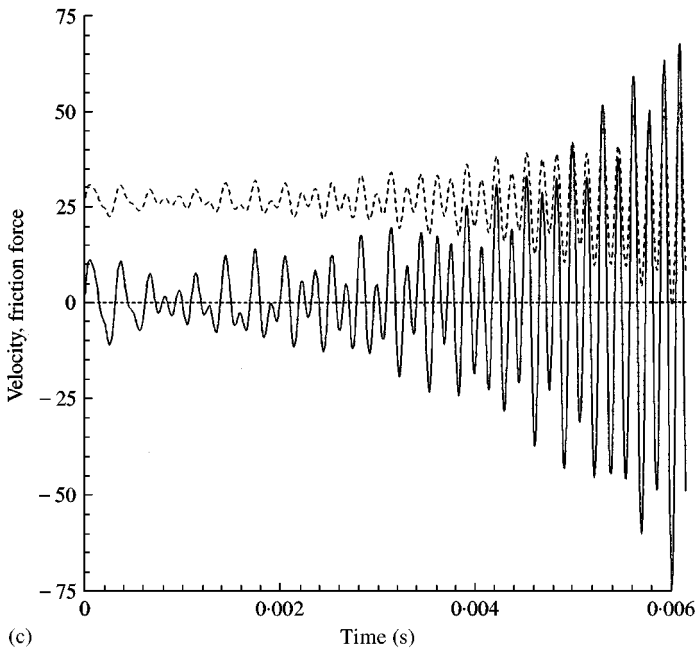


Figure 7. Continued.

with various values for  $\gamma$ , where  $\eta_{mn}$  were kept constant, showed that an increase in  $\gamma$  is destabilizing for all modes. No instability occurs if  $\gamma = 0$ .

For a real model wheel, the loss factors of the individual modes are unlikely to differ by over a factor 10 as assumed here (see Table 2). Less extreme differences

yield time histories with the same qualitative behaviours. However, the amplitude growth then becomes visible only over much longer time intervals, and this is hard to show in figures of time histories.

Generally, it is not easy to recognize different modes in a time history and to determine which modes are stable and which are unstable. The stability behaviour of individual modes can be studied more systematically by an analysis in the frequency domain; this will be addressed in a companion paper [12].

Simulations using the non-linear friction characteristic (5.2), which describes stick/slip, lead to limit cycle oscillations (see Figures 8(a)–(d)). They all have the same limit cycle amplitude, but different limit cycle frequencies. Figure 8(a) shows the case where the amplitude of mode (2, 1) grows and eventually a limit cycle with the frequency of that mode develops. Figure 8(b) shows the same phenomenon for

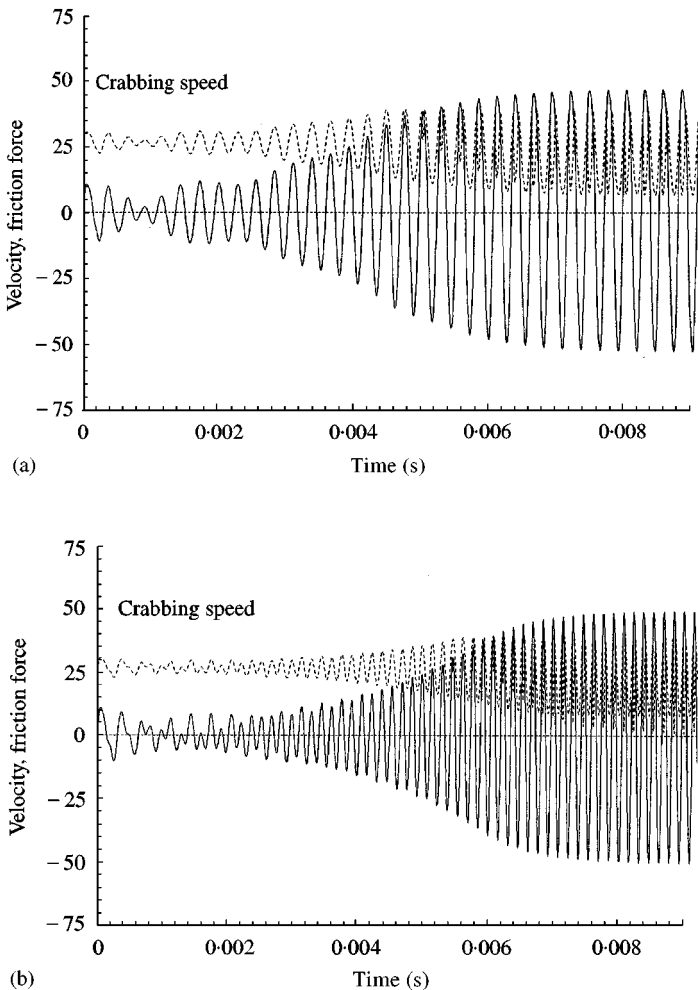


Figure 8. Time histories of the disc velocity (solid curve) and friction force (dashed curve); stick/slip friction characteristic.

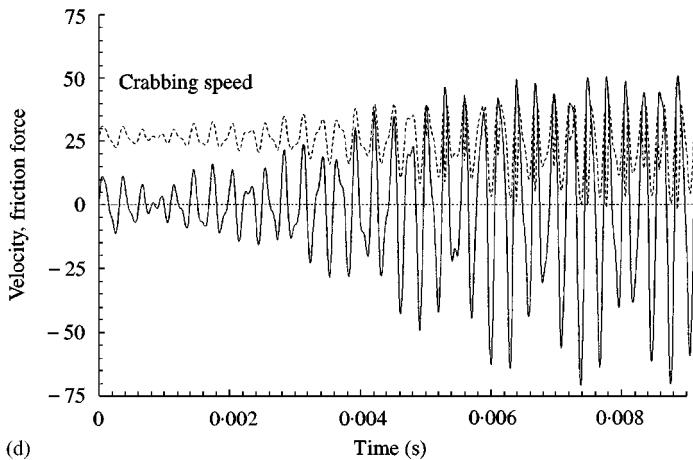
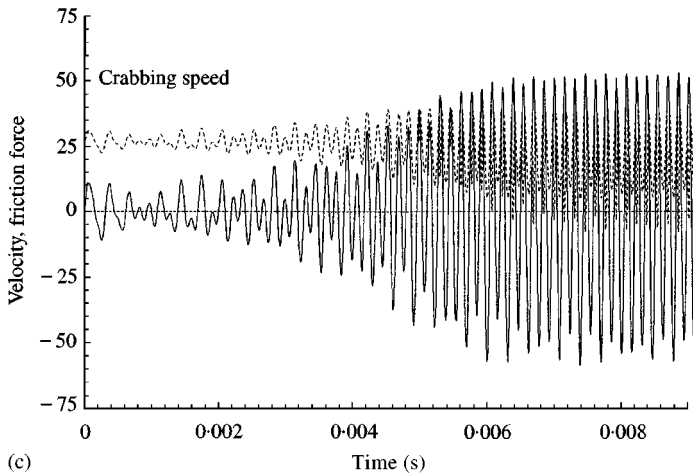


Figure 8. Continued.

mode (3, 1). In Figure 8(c) both modes are unstable at first, with mode (3, 1) dominating; later, in the limit cycle, there is only one frequency which is that of mode (3, 1). Figure 8(d) shows the case where both modes (2, 1) and (3, 1) are about equally unstable at first; the limit cycle that develops has the frequency of mode (2, 1).

The amplitude limit is imposed by the stick section of the friction characteristic which, in contrast to the slip section, has a stabilizing effect. The velocity in the stick section is similar to the crabbing speed  $V$ , and this is the amplitude of the limit cycle oscillations. The crabbing speed was fixed at  $V = 50 \times 10^{-6}$  m/s in Figure 8(a)–(d).

It is not possible to draw firm conclusions about the limit cycle frequencies without a systematic study of the non-linear interaction between modes. All that can be said at this stage is that if there are two unstable modes, with one of them dominating, the dominating one will determine the limit cycle frequency.

TABLE 2

*Modal loss factors used for the numerical simulations shown in Figures 7(a)–(d) and 8(a)–(d)*

<i>m</i>	<i>n</i>	$\eta_{mn}$ Figures 7(a), 8(a)	$\eta_{mn}$ Figures 7(b), 8(b)	$\eta_{mn}$ Figures 7(c), 8(c)	$\eta_{mn}$ Figures 7(d), 8(d)
0	1	0.07	0.07	0.07	0.07
1	1	0.07	0.07	0.07	0.07
2	1	0.007	0.07	0.02	0.008
3	1	0.07	0.004	0.002	0.006
4	1	0.07	0.07	0.07	0.07

## 6. CONCLUSIONS

From a mathematical point of view, curve squeal is an unstable wheel oscillation which turns into a limit cycle. This was shown in the present paper which modelled the wheel with a flat circular disc and the wheel/rail interaction with a stick/slip friction force, where stick occurs if the wheel velocity becomes equal or similar to the crabbing speed (the speed of the constant lateral motion of a wheel across the rail while traversing a curve).

The numerical simulations based on our model produce time histories for the disc velocity with two distinctly different stages. In the first stage there is an unstable growth of the amplitudes. The velocity and friction force are in phase and proportional to each other; the velocity is less than the crabbing speed, i.e., there is slip but no stick. In the second stage of the time history, the disc velocity reaches the crabbing speed and a stick/slip oscillation sets in. This is a limit cycle oscillation with a velocity amplitude which is equal (or very similar) to the crabbing speed. The limit cycle amplitude determines the intensity of the squeal. It is the slip section (sliding friction) of the friction characteristic which is responsible for the instability, and the stick section (rolling friction) which is responsible for the limit cycle.

Several wheel modes may play a part in the stability behaviour and the limit cycle. Whether or not an individual mode is unstable depends strongly on the damping of that mode; if the modal loss factor is sufficiently high, the mode will remain stable. Only a vague criterion is available at this stage as to which modes determine the limit cycle frequency. If there is only one unstable mode, or several unstable modes with one of them dominating, then that mode will determine the limit cycle frequency.

The calculations shown here were performed in the time domain, rather than the frequency domain. An analysis in the frequency domain would give more insight into the behaviour of individual modes. A linear analysis would give the growth rates of individual modes, indicating immediately whether a mode is stable or unstable. This will be reported in a companion paper. A non-linear analysis, taking

the full stick/slip friction characteristic into account and any modal interactions caused by this, might shed some light on the selection of a particular mode for the limit cycle frequency.

Our predictions are in agreement with the more phenomenological findings of earlier authors (see, for example, references [1] and [13]), and in particular with the proposed means for the elimination and reduction of curve squeal.

Curve squeal can be eliminated if the unstable amplitude growth can be prevented. This has been achieved in practice by increasing the wheel damping (equivalent to increasing the modal loss factors in our model). It has also been achieved by applying lubrication to change the properties of the wheel/rail interface in such a way that the slope of the decreasing section of the creep curve is lessened (equivalent to changing the friction characteristic in our model in such a way that the gradient of the slip section is reduced). Curve squeal can be reduced in intensity by lowering the limit cycle amplitude. This is typically achieved by reducing the train speed and by increasing the curve radius; both measures reduce the crabbing speed which, according to our model, determines the velocity amplitude of the limit cycle. Another method of eliminating curve squeal is the use of train vehicles which are designed in such a way that wheel crabbing in curves does not occur. This has been achieved, for example, by the use of bogies with steerable wheelsets and, in some cases, with independent wheels.

A companion paper [14] will present a completely new method of eliminating curve squeal. This method involves a feedback system to prevent the unstable wheel oscillations; it is a special form of active control.

#### ACKNOWLEDGMENT

The research described in this paper was supported by the Engineering and Physical Sciences Research Council of the UK (EPSRC grant number GR/H73776).

#### REFERENCES

1. M. J. RUDD 1976 *Journal of Sound and Vibration* **46**, 381–394. Wheel/rail noise—Part II: Wheel squeal.
2. M. E. MCINTYRE and J. WOODHOUSE 1979 *Acustica* **43**, 93–108. On the fundamentals of bowed-string dynamics.
3. H. VON STAPPENBECK 1954 *Zeitschrift VDI* **96**, 171–175. Das Kurvengeräusch der Straßenbahn—Möglichkeiten zu seiner Unterdrückung.
4. P. J. REMINGTON 1985 *Journal of Sound and Vibration* **116**, 339–353. Wheel/rail squeal and impact noise: What do we know? What don't we know? Where do we go from here?
5. E. SCHNEIDER, K. POPP and H. IRRETIER 1988 *Journal of Sound and Vibration* **120**, 227–244. Noise generation in railway wheels due to rail-wheel contact forces.
6. U. FINGBERG 1990 *Journal of Sound and Vibration* **143**, 365–377. A model of wheel-rail squealing noise.
7. F. PÉRIARD 1998 *Ph.D. Dissertation, Technische Universiteit Delft*; ISBN 90-9011964-7, NUGI 834. Wheel-rail noise generation: curve squealing by trams.
8. K. POPP and P. STELTER 1990 *Philosophical Transactions of the Royal Society London A* **332**, 89–105. Stick-slip vibrations and chaos.

9. A. J. McMILLAN 1997 *Journal of Sound and Vibration* **205**, 323–335. A non-linear friction model for self-excited vibrations.
10. LORD RAYLEIGH 1896 *The Theory of Sound*, Vol. 1. New York: Dover Publications, second edition, 1945 re-issue.
11. M. ABRAMOWITZ and I. A. STEGUN 1972 *Handbook of Mathematical Functions*. New York: Dover Publications.
12. M. A. HECKL 2000 *Journal of Sound and Vibration* **229**, 695–707. Curve squeal of train wheels, Part 2: Which wheel modes are prone to squeal?
13. M. HECHT 1995 *Schweizer Eisenbahn-Revue* **3**, 102–108. Kurvenkreischen-Ursachen und Gegenmassnahmen.
14. M. A. HECKL and X. Y. HUANG 2000 *Journal of Sound and Vibration* **229**, 709–735. Curve squeal of train wheels, Part 3: Active control.
15. I. D. ABRAHAMS 1994 *Personal Communication*. Check on eigenfunctions of free-edged disc.

## APPENDIX A: THEORETICAL CALCULATION OF THE GREEN'S FUNCTION OF AN ANNULAR DISC

The required Green's function  $G$  is the solution of the boundary value problem specified by equations (3.1) and (3.2a)–(3.2d).  $G$  will be determined in three steps. The first two steps follow Rayleigh's studies [reference 10, pp. 359–363] which considered a somewhat simpler case, a circular disc (no inner edge, no clamping), and calculated its eigenfunctions. Complex notation is used for the Green's function with the understanding that only the real part is relevant.

### A.1. SEPARATION OF VARIABLES TO SOLVE THE UNFORCED PROBLEM

The homogeneous version of equation (3.1),

$$B\nabla^4 G + M \frac{\partial^2 G}{\partial t^2} = 0, \quad (\text{A1})$$

is assumed to have a solution with a harmonic time dependence,

$$G(r, \varphi, t) = g(r, \varphi) e^{-i\omega t}, \quad (\text{A2})$$

then equation (A1) becomes

$$(\nabla^2 + k^2)(\nabla^2 - k^2) g(r, \varphi) = 0, \quad \text{with} \quad k^2 = \omega \sqrt{\frac{M}{B}}. \quad (\text{A3a, b})$$

One can conclude from equation (A3a) that  $g(r, \varphi)$  is a solution of the two equations

$$\nabla^2 g + k^2 g = 0 \quad \text{and} \quad \nabla^2 g - k^2 g = 0. \quad (\text{A4a, b})$$

The variables  $r$  and  $\varphi$  are separated by assuming

$$g(r, \varphi) = R(r)\Phi(\varphi). \tag{A5}$$

This leads from equation (A4), and with

$$\nabla^2 g = \Phi \frac{\partial^2 R}{\partial r^2} + \Phi \frac{1}{r} \frac{\partial R}{\partial r} + \frac{R}{r^2} \frac{\partial^2 \Phi}{\partial \varphi^2}, \tag{A6}$$

to the following ordinary differential equations for the functions  $\Phi$  and  $R$ :

$$\frac{\partial^2 \Phi}{\partial \varphi^2} + m^2 \Phi = 0 \tag{A7}$$

and

$$r^2 \frac{\partial^2 R}{\partial r^2} + r \frac{\partial R}{\partial r} + (-m^2 \pm k^2 r^2) R = 0. \tag{A8}$$

Equation (A7) has sinusoidal solutions. The point force, yet to be considered, imposes a symmetry of the disc motion (see Figure 4) with respect to the line connecting the force point  $(r', \varphi')$  to the origin  $(0, 0)$ , so only symmetrical solutions are of interest here,

$$\Phi(\varphi) = \cos m(\varphi - \varphi'), \quad m = 0, 1, 2, 3, \dots \tag{A9}$$

Equation (A8) is the differential equation for the Bessel functions  $J_m, Y_m$  (upper sign, see equation 9.1.1 in reference [11]) and for the hyperbolic Bessel functions  $I_m, K_m$  (lower sign, see equation 9.6.1 in reference [11]). Its general solution is

$$R(r) = A[J_m(kr) + BI_m(kr) + CY_m(kr) + DK_m(kr)]. \tag{A10}$$

Equations (A2), (A5), (A9) and (A10) can now be combined to give

$$G(r, \varphi, t) = A \cos m(\varphi - \varphi') [J_m(kr) + BI_m(kr) + CY_m(kr) + DK_m(kr)] e^{-i\omega t}, \tag{A11}$$

where the allowed wave numbers  $k$  and the relative amplitudes  $B, C$  and  $D$  will be determined from the boundary conditions.  $A$  will be determined when considering the forced problem.

A.2. APPLICATION OF THE BOUNDARY CONDITIONS

Substitution of equation (A11) into the boundary conditions (3.2a)–(3.2d) gives

$$J_m(kb) + BI_m(kb) + CY_m(kb) + DK_m(kb) = 0, \tag{A12a}$$

$$J'_m(kb) + BI'_m(kb) + CY'_m(kb) + DK'_m(kb) = 0, \tag{A12b}$$

$$\begin{aligned} &(ka)^2 [J''_m(ka) + BI''_m(ka) + CY''_m(ka) + DK''_m(ka)] \\ &+ vka [J'_m(ka) + BI'_m(ka) + CY'_m(ka) + DK'_m(ka)] \\ &- vm^2 [J_m(ka) + BI_m(ka) + CY_m(ka) + DK_m(ka)] = 0, \end{aligned} \tag{A12c}$$

$$\begin{aligned} &(ka)^3 [J'''_m(ka) + BI'''_m(ka) + CY'''_m(ka) + DK'''_m(ka)] \\ &+ (ka)^2 [J''_m(ka) + BI''_m(ka) + CY''_m(ka) + DK''_m(ka)] \\ &- ka[1 + (2 - v)m^2] [J'_m(ka) + BI'_m(ka) + CY'_m(ka) + DK'_m(ka)] \\ &+ (3 - v)m^2 [J_m(ka) + BI_m(ka) + CY_m(ka) + DK_m(ka)] = 0. \end{aligned} \tag{A12d}$$

The primes denote derivatives of the Bessel functions. This is a set of 4 coupled equations for the unknowns  $B$ ,  $C$  and  $D$  (linear) and  $k$  (non-linear). The process of obtaining a separate equation for each of the unknowns is lengthy, but straightforward. From the first two equations, equations (A12a, b), one obtains by elimination of  $D$  and  $C$

$$C = \frac{T_{JK} + BT_{IK}}{T_{KY}} \quad \text{and} \quad D = \frac{T_{YJ} + BT_{YI}}{T_{KY}}, \tag{A13a, b}$$

with

$$T_{JK} = J'_m(kb)K_m(kb) - J_m(kb)K'_m(kb), \tag{A14a}$$

$$T_{IK} = I'_m(kb)K_m(kb) - I_m(kb)K'_m(kb), \tag{A14b}$$

$$T_{KY} = K'_m(kb)Y_m(kb) - K_m(kb)Y'_m(kb), \tag{A14c}$$

$$T_{YJ} = Y'_m(kb)J_m(kb) - Y_m(kb)J'_m(kb), \tag{A14d}$$

$$T_{YI} = Y'_m(kb)I_m(kb) - Y_m(kb)I'_m(kb). \tag{A14e}$$

If these expressions are substituted into the third equation, equation (A12c), an explicit expression for  $B$  can be found,

$$B = -\frac{T_J T_{KY} + T_Y T_{JK} + T_K T_{YJ}}{T_I T_{KY} + T_Y T_{IK} + T_K T_{YI}}, \quad (\text{A15})$$

with

$$T_J = k^2 J_m''(ka) + \frac{v}{a} k J_m'(ka) - \frac{v}{a^2} J_m(ka), \quad (\text{A16a})$$

$$T_Y = k^2 Y_m''(ka) + \frac{v}{a} k Y_m'(ka) - \frac{v}{a^2} Y_m(ka), \quad (\text{A16b})$$

$$T_K = k^2 K_m''(ka) + \frac{v}{a} k K_m'(ka) - \frac{v}{a^2} K_m(ka), \quad (\text{A16c})$$

$$T_I = k^2 I_m''(ka) + \frac{v}{a} k I_m'(ka) - \frac{v}{a^2} I_m(ka). \quad (\text{A16d})$$

The fourth equation, equation (A12d), can be written as

$$BS_I + CS_Y + DS_K + S_J = 0, \quad (\text{A17})$$

with

$$S_I = (ka)^3 I_m'''(ka) + (ka)^2 I_m''(ka) - [1 + (2 - v)m^2] ka I_m'(ka) + (3 - v)m^2 I_m(ka), \quad (\text{A18a})$$

$$S_Y = (ka)^3 Y_m'''(ka) + (ka)^2 Y_m''(ka) - [1 + (2 - v)m^2] ka Y_m'(ka) + (3 - v)m^2 Y_m(ka), \quad (\text{A18b})$$

$$S_K = (ka)^3 K_m'''(ka) + (ka)^2 K_m''(ka) - [1 + (2 - v)m^2] ka K_m'(ka) + (3 - v)m^2 K_m(ka), \quad (\text{A18c})$$

$$S_J = (ka)^3 J_m'''(ka) + (ka)^2 J_m''(ka) - [1 + (2 - v)m^2] ka J_m'(ka) + (3 - v)m^2 J_m(ka). \quad (\text{A18d})$$

Substitution for  $B$ ,  $C$  and  $D$  with the  $k$ -dependent expressions (A15), (A13a) and (A13b), respectively, turns equation (A17) into an equation for  $k$ ; its roots,  $k_{mn}$ , are the allowed wave numbers, numbered by the integer  $n = 1, 2, 3, \dots$ . They are best

determined by a numerical approach such as root bracketing combined with the Newton/Raphson method. With  $k_{mn}$  known, the relative amplitudes  $B$ ,  $C$  and  $D$  can be calculated from equations (A15) and (A13a, b) to give  $B_{mn}$ ,  $C_{mn}$  and  $D_{mn}$ . The eigenfunctions  $G_{mn}(r, \varphi, t)$ , which describe the free vibrations of the disc, can then be written with equation (A11) as

$$G_{mn}(r, \varphi, t) = \cos m(\varphi - \varphi') R_{mn}(r) e^{-i\omega_{mn}t}, \tag{A19}$$

where

$$R_{mn}(r) = J_m(k_{mn}r) + B_{mn}I_m(k_{mn}r) + C_{mn}Y_m(k_{mn}r) + D_{mn}K_m(k_{mn}r), \tag{A20a}$$

and (from equation (A3b))

$$\omega_{mn} = k_{mn}^2 \sqrt{\frac{B}{M}}. \tag{A20b}$$

### A.3. SOLUTION OF THE FORCED PROBLEM

We assume that the solution of the forced problem is of the form

$$G = \begin{cases} \sum_{m=0}^{\infty} \sum_{n=1}^{\infty} A_{mn} \cos m(\varphi - \varphi') R_{mn}(r) e^{-i\omega_{mn}(t-t')} & \text{for } t \geq t', \\ 0 & \text{for } t < t', \end{cases} \tag{A21}$$

where  $R_{mn}(r)$  and  $\omega_{mn}$  are given by equation (A20a, b).

The aim is now to determine the coefficients  $A_{mn}$  in equation (A21). For this purpose, the governing equation (3.1) is integrated with respect to time, over a small interval  $(t' - \varepsilon, t' + \varepsilon)$  centred around the excitation time  $t'$ ,

$$\int_{t'-\varepsilon}^{t'+\varepsilon} \left( B\nabla^4 G + M \frac{\partial^2 G}{\partial t^2} \right) dt = \delta(r - r') \delta(\varphi - \varphi'). \tag{A22}$$

If the limit  $\varepsilon \rightarrow 0$  is taken, the integral over the  $\nabla^4 G$  term tends to zero, and

$$M \lim_{\varepsilon \rightarrow 0} \left( \frac{\partial G}{\partial t} \Big|_{t=t'+\varepsilon} - \frac{\partial G}{\partial t} \Big|_{t=t'-\varepsilon} \right) = \delta(r - r') \delta(\varphi - \varphi'). \tag{A23}$$

Substitution for  $G$ , using the time derivative of both parts of equation (A21), gives

$$M \sum_{m=0}^{\infty} \sum_{n=1}^{\infty} -i\omega_{mn} A_{mn} \cos m(\varphi - \varphi') R_{mn}(r) = \delta(r - r') \delta(\varphi - \varphi'). \tag{A24}$$

The  $(r, \varphi)$ -dependent parts of the eigenfunctions,  $\cos m(\varphi - \varphi') R_{mn}(r)$ , are orthogonal [15], hence

$$\int_{\varphi=0}^{2\pi} \int_{r=b}^a \cos m(\varphi - \varphi') \cos m'(\varphi - \varphi') R_{mn}(r) R_{m'n'}(r) r \, dr \, d\varphi \sim \delta_{mm'} \delta_{nn'}. \quad (\text{A25})$$

This allows one to calculate the coefficients  $A_{mn}$  by multiplying both sides of equation (A24) by  $\cos m'(\varphi - \varphi') R_{m'n'}(r)$  and integrating over the area of the disc,

$$\begin{aligned} M \sum_{m=0}^{\infty} \sum_{n=1}^{\infty} -i\omega_{mn} A_{mn} \int_{\varphi=0}^{2\pi} \int_{r=b}^a \cos m(\varphi - \varphi') \cos m'(\varphi - \varphi') R_{mn}(r) R_{m'n'}(r) r \, dr \, d\varphi \\ = r' R_{m'n'}(r'). \end{aligned} \quad (\text{A26})$$

Because of equation (A25), only the terms  $m = m'$  and  $n = n'$  contribute to the sums in equation (A26), and an explicit expression for  $A_{mn}$  is obtained,

$$A_{mn} = \frac{r' R_{mn}(r')}{-Mi\omega_{mn} \int_{\varphi=0}^{2\pi} \int_{r=b}^a [\cos m(\varphi - \varphi') R_{mn}(r)]^2 r \, dr \, d\varphi}. \quad (\text{A27})$$

The double integral in the denominator can be reduced to a single integral over  $r$  if the integration over  $\varphi$  is performed

$$\int_{\varphi=0}^{2\pi} \cos^2 m(\varphi - \varphi') \, d\varphi = \varepsilon_m \pi \quad \text{with} \quad \varepsilon_m = \begin{cases} 2 & \text{for } m = 0, \\ 1 & \text{for } m \neq 0, \end{cases} \quad (\text{A28})$$

and this leads to equation (3.6a) for  $A_{mn}$  stated in the main text. The remaining integral over  $r$  is best calculated numerically.